

A *SPITZER* INFRARED SPECTROGRAPH SPECTRAL SEQUENCE OF M, L, AND T DWARFS

MICHAEL C. CUSHING,^{1,2} THOMAS L. ROELLIG,³ MARK S. MARLEY,⁴ D. SAUMON,⁵ S. K. LEGGETT,⁶ J. DAVY KIRKPATRICK,⁷
JOHN C. WILSON,⁸ G. C. SLOAN,⁹ AMY K. MAINZER,¹⁰ JEFF E. VAN CLEVE,¹¹ AND JAMES R. HOUCK¹²

Received 2006 February 21; accepted 2006 May 5

ABSTRACT

We present a low-resolution ($R \equiv \lambda/\Delta\lambda \approx 90$), 5.5–38 μm spectral sequence of a sample of M, L, and T dwarfs obtained with the Infrared Spectrograph (IRS) on board the *Spitzer Space Telescope*. The spectra exhibit prominent absorption bands of H_2O at 6.27 μm , CH_4 at 7.65 μm , and NH_3 at 10.5 μm and are relatively featureless at $\lambda \gtrsim 15 \mu\text{m}$. Three spectral indices that measure the strengths of these bands are presented; H_2O absorption features are present throughout the MLT sequence, while the CH_4 and NH_3 bands first appear at roughly the L/T transition. Although the spectra are, in general, qualitatively well matched by synthetic spectra that include the formation of spatially homogeneous silicate and iron condensate clouds, the spectra of the mid-type L dwarfs show an unexpected flattening from roughly 9 to 11 μm . We hypothesize that this may be a result of a population of small silicate grains that are not predicted in the cloud models. The spectrum of the peculiar T6 dwarf 2MASS J0937+2931 is suppressed from 5.5 to 7.5 μm relative to typical T6 dwarfs and may be a consequence of its mildly metal-poor/high surface gravity atmosphere. Finally, we compute bolometric luminosities of a subsample of the M, L, and T dwarfs by combining the IRS spectra with previously published 0.6–4.1 μm spectra and find good agreement with the values of Golimowski et al., who use L' - and M' -band photometry to account for the flux emitted at $\lambda > 2.5 \mu\text{m}$.

Subject headings: infrared: stars — stars: late-type — stars: low-mass, brown dwarfs

1. INTRODUCTION

The discovery of the first bona fide brown dwarf (BD) Gl 229B (Nakajima et al. 1995) and the confirmation of other BD candidates (Basri et al. 1996; Rebolo et al. 1996) ushered in a new era in both stellar and planetary astrophysics, since BDs bridge the gap in mass between stars and planets. Over 400 very low mass stars and BDs, collectively known as “ultracool” dwarfs, have since been discovered, primarily in wide-field optical and near-infrared surveys such as the Two Micron All Sky Survey (2MASS; Skrutskie et al. 2006), the Deep Near Infrared Southern Sky Survey (DENIS; Epchtein et al. 1997), and the Sloan Digital Sky Survey (SDSS; York et al. 2000). Ultracool dwarfs have effective temperatures (T_{eff}) less than ~ 2700 K and spectral types later than $\sim \text{M7 V}$, and include the new L and T dwarfs. Since their spectral energy distributions (SEDs) peak near $\sim 1 \mu\text{m}$, considerable observational (Basri 2000; Kirkpatrick 2005) and theo-

retical (Chabrier & Baraffe 2000; Burrows et al. 2001) effort has gone into studying them at both red-optical and near-infrared wavelengths.

Nevertheless, observations at $\lambda > 2.5 \mu\text{m}$ can also provide important constraints on the fundamental parameters and atmospheric physics of ultracool dwarfs. For example, the T_{eff} of an ultracool dwarf is typically determined by combining an observational bolometric luminosity with a theoretical radius (e.g., Dahn et al. 2002; Golimowski et al. 2004). Since spectroscopic observations are typically limited to $\lambda \lesssim 2.5 \mu\text{m}$, the T_{eff} scale therefore depends critically on an accurate accounting of the flux emitted at longer wavelengths. The effects of nonequilibrium chemistry on the abundances of CO, CH_4 , N_2 , and NH_3 due to the vertical transport of gas within the atmospheres of ultracool dwarfs, and hence the band strengths of CO, CH_4 , and NH_3 , are also strongest at these wavelengths (Saumon et al. 2003a, 2003b). In addition, observations at $\lambda > 2.5 \mu\text{m}$ are easier to interpret using atmospheric models because the dominant absorption bands (H_2O , CO, CH_4 , and NH_3) at these wavelengths arise from fundamental transitions with nearly complete line lists compared to the overtone and combination bands at near-infrared wavelengths. Finally, mid-infrared spectroscopy adds important information about the vertical structure and properties of atmospheric condensates. In principle, Mie scattering effects of iron and silicate grains expected in the atmospheres of the L dwarfs allow constraints to be placed on particle sizes, but only with spectra obtained over a large wavelength range. In addition, if a population of small particles is present, silicate absorption features may be apparent near 10 μm .

Unfortunately, observations of ultracool dwarfs at $\lambda > 2.5 \mu\text{m}$ are not as common as they are at shorter wavelengths, due to the difficulty of observing from the ground at these wavelengths. The majority of the observations consist of L' - and M' -band photometry (Stephens et al. 2001; Leggett et al. 2002; Golimowski et al. 2004), although some spectroscopy has been performed at these wavelengths (Noll et al. 1997, 2000; Oppenheimer et al. 1998; Burgasser 2001; Cushing et al. 2005). In particular, the ν_3

¹ Steward Observatory, University of Arizona, 933 North Cherry Avenue, Tucson, AZ 85721; mcushing@as.arizona.edu.

² Spitzer Fellow.

³ NASA Ames Research Center, Mail Stop 245-6, Moffett Field, CA 94035; thomas.roellig@nasa.gov.

⁴ NASA Ames Research Center, Mail Stop 254-3, Moffett Field, CA 94035; mmarley@mail.arc.nasa.gov.

⁵ Los Alamos National Laboratory, Applied Physics Division, Mail Stop P365, Los Alamos, NM 87544; dsaumon@lanl.gov.

⁶ Gemini Northern Operations, 670 North A’ohoku Place, Hilo, HI 96720; s.leggett@jach.hawaii.edu.

⁷ Infrared Processing and Analysis Center, California Institute of Technology, Mail Stop 100-22, Pasadena, CA 91125; davy@ipac.caltech.edu.

⁸ Astronomy Building, University of Virginia, 530 McCormick Road, Charlottesville, VA 22903; jcw6z@virginia.edu.

⁹ Astronomy Department, Cornell University, Ithaca, NY 14853; sloan@isc.astro.cornell.edu.

¹⁰ Jet Propulsion Laboratory, Mail Stop 169-506, 4800 Oak Grove Drive, Pasadena, CA 91109; amainzer@jpl.nasa.gov.

¹¹ Ball Aerospace and Technologies Corporation, 1600 Commerce Street, Boulder, CO 80301; jvanclev@ball.com.

¹² Astronomy Department, Cornell University, Ithaca, NY 14853; jrh13@cornell.edu.

fundamental band of CH₄ at $\sim 3.3 \mu\text{m}$ has been detected in the spectra of L and T dwarfs (Oppenheimer et al. 1998; Burgasser 2001; Noll et al. 2000; Cushing et al. 2005), and the fundamental CO band at $\sim 4.7 \mu\text{m}$ has been detected in the T dwarf Gl 229B (Noll et al. 1997; Oppenheimer et al. 1998). Even fewer ground-based observations of ultracool dwarfs exist at $\lambda > 5 \mu\text{m}$ and are limited to photometric observations (Matthews et al. 1996; Creech-Eakman et al. 2004; Sterzik et al. 2005) of just a few dwarfs.

The launch of the *Spitzer Space Telescope* (Werner et al. 2004), which is sensitive from 3.6 to 160 μm , has opened a heretofore untapped wavelength range for the study of ultracool dwarfs. In particular, the Infrared Array Camera (IRAC; Fazio et al. 2004) and the IRS (Houck et al. 2004) are providing unprecedented photometric and spectroscopic observations of ultracool dwarfs at mid-infrared wavelengths. Roellig et al. (2004) presented the first mid-infrared spectra of an M, L, and T dwarf and identified absorption bands of H₂O, CH₄, and NH₃. In this paper we extend the work of Roellig et al. and present a 5.3–38 μm spectral sequence of M, L, and T dwarf spectra obtained with the IRS. Forthcoming papers will provide a more in-depth analysis of the spectra. We describe the observations, data reduction, and absolute flux calibration of the spectra in § 2, while in § 3 we discuss the spectra sequence, derive three spectral indices that measure the strengths of the H₂O, CH₄, and NH₃ bands, and discuss a number of interesting objects. In § 4 we present full 0.6–15 μm SEDs of a subsample of M, L, and T dwarfs and compute their bolometric luminosities.

2. OBSERVATIONS AND DATA REDUCTION

Our current sample consists of 14 M dwarfs, 21 L dwarfs, and 11 T dwarfs drawn from the literature.¹³ The observations were conducted with the IRS as part of the “Dim Suns” IRS Science Team Guaranteed Time Observation (GTO) program. The IRS is composed of four modules capable of performing low ($R \equiv \lambda/\Delta\lambda \approx 90$) to moderate resolution ($R \approx 600$) spectroscopy from 5.3 to 38 μm . We used the Short-Low (SL) module that covers from 5.3 to 15.3 μm at $R \approx 90$ in 2 orders, and the Long-Low (LL) module that covers from 14.0 to 38 μm at $R \approx 90$, also in 2 orders. A log of the observations, including the *Spitzer* AOR key, spectroscopic module, and total on-source integration time, is given in Table 1. Although both optical and infrared spectral types are listed in Table 1, we hereafter use optical types for the M and L dwarfs (Kirkpatrick et al. 1991, 1999) and infrared types for the T dwarfs (Burgasser et al. 2006b) unless otherwise noted. In addition, we hereafter abbreviate the numerical portions of the 2MASS, SDSS, and DENIS target designations as Jhhmm ± ddm, where the suffix is the sexagesimal right ascension (hours and minutes) and declination (degrees and arcminutes) at J2000.0 equinox.

The observations consisted of a series of exposures obtained at two positions along each slit. The raw IRS data were processed with the IRS pipeline (version S12) at the *Spitzer* Science Center. The data were reduced using custom IDL procedures based on the Spextool (Cushing et al. 2004) data reduction package. The background signal was first removed from each science frame by subtracting the median of the frames obtained in the same spectroscopic module but with the target in the other order. Any residual background was removed by subtracting off the median signal in the slit at each column, excluding regions that contain signal from the target. The spectra were then extracted with a fixed-width aperture (6'' in the SL module and 9'' in the LL module) and wavelength calibrated using the technique employed

by the IRS data reduction package, the Spectroscopic Modeling Analysis and Reduction Tool (SMART; Higdón et al. 2004).

Observations of standard stars obtained as part of the normal IRS calibration observations were used to remove the instrument response function and flux calibrate the science targets. We used α Lac (A0 V) to correct the SL spectra and HR 6348 (K1 III) for the LL spectra. The standard star spectra were extracted in a fashion similar to that used for the science targets. Model spectra of the two standard stars from Cohen et al. (2003) were used to remove the intrinsic SED from the raw standard star spectra. The spectra from the SL module were then merged into a single 5.3–15.3 μm spectrum, and the spectra from the LL module were merged into a single 14.0–38 μm spectrum. Finally, for those targets with both SL and LL data, the spectra from the two modules are merged together; any offset in the flux density levels of the two spectra is removed by scaling the LL spectrum to the flux density level of the SL spectrum.

The final step in the reduction process is to absolutely flux calibrate the spectra using IRAC Band 4 photometry. Fortunately, 27 of the dwarfs in our sample have been observed as part of an IRAC Science Team GTO program (Patten et al. 2006). Below we describe the process used to absolutely flux calibrate the dwarf spectra in our sample.

IRAC observations are reported as a flux density, $f_{\nu}^{\text{IRAC}}(\lambda_0)$, at a nominal wavelength λ_0 ($\lambda_0 = 7.872 \mu\text{m}$ for Band 4 [Reach et al. 2005]) assuming the target has a SED given by

$$\tilde{\nu}f_{\nu}(\nu) = \text{constant} = \nu_0 f_{\nu}^{\text{IRAC}}(\lambda_0), \quad (1)$$

where $\nu_0 = c/\lambda_0$. If this assumption is invalid, as it is for ultracool dwarfs, then the quoted flux density is not the flux density of the target at λ_0 . Therefore, in order to compare an IRAC observation to an IRS spectrum, we must compute an equivalent $f_{\nu}^{\text{IRAC}}(\lambda_0)$, given the IRS spectrum.

The value of $f_{\nu}^{\text{IRAC}}(\lambda_0)$ is determined for any source with a SED given by $f_{\nu}(\lambda)$ from the requirement that the number of electrons detected per second from the source, N_e , be equal to the number of electrons detected per second from a hypothetical target with a SED given by equation (1), \tilde{N}_e . That is,

$$A \int \frac{\tilde{f}_{\nu}(\nu)}{h\nu} S(\nu) d\nu = A \int \frac{f_{\nu}(\nu)}{h\nu} S(\nu) d\nu, \quad (2)$$

where A is the area of the telescope and $S(\nu)$ is the system response function of the telescope plus instrument plus detector system in units of photons electron⁻¹. Substituting equation (1) into equation (2), and solving for $f_{\nu}^{\text{IRAC}}(\lambda_0)$, we find

$$f_{\nu}^{\text{IRAC}}(\lambda_0) = \frac{\int (\nu_0/\nu) f_{\nu}(\nu) S(\nu) d\nu}{\int (\nu_0/\nu)^2 S(\nu) d\nu}. \quad (3)$$

Equation (3) can be used to predict the flux density IRAC would report if it were to observe a source with a SED given by $f_{\nu}(\nu)$.

The IRS spectra of the dwarfs with IRAC observations were absolutely flux calibrated by multiplying each spectrum by a scale factor C , given by

$$C = \frac{f_{\nu}^{\text{IRAC}}(\lambda_0)}{f_{\nu}^{\text{IRS}}(\lambda_0)}, \quad (4)$$

where $f_{\nu}^{\text{IRS}}(\lambda_0)$ was determined using the IRS spectrum and equation (4), and $f_{\nu}^{\text{IRAC}}(\lambda_0)$ is the reported IRAC flux density for the dwarf in question. The correction factors ranged from

¹³ Databases of known L and T dwarfs can be found at <http://DwarfArchives.org> and <http://www.jach.hawaii.edu/~skf/LTdata.html>.

TABLE 1
LOG OF THE IRS OBSERVATIONS

OBJECT	OPTICAL SPECTRAL TYPE ^a	INFRARED SPECTRAL TYPE ^a	AOR KEY	EXPOSURE TIME ^b (s)			
				SL2	SL1	LL2	LL1
GI 229A	M1 V	...	4185856	12	12	30	30
GI 1	M1.5 V	...	3873792	24	24
G 196-3A	M2.5 V	...	3879168	30	120	1220	120
GI 674	M2.5 V	...	3874304	24	24
GI 752A	M2.5 V	...	3876864 ^c	30	30	488	488
GI 687	M3 V	...	3874560	24	24
GI 849	M3.5 V	...	3873024	24	24
GJ 1001A	M3.5 V	...	4190464 ^d	484	484	488	976
GI 866ABC	M5 V	...	3878912	24	24	24	24
GI 65AB	M5.5 V	...	3878400	24	24	24	24
GJ 1111	M6.5 V	...	3876096	24	24
LHS 3003	M7 V	...	3876608	30	30	732	732
vB 10	M8 V	...	12486401	60	60	488	488
BRI 0021-0214	M9.5 V	...	3877632	122	244
2MASS J07464256+2000321AB	L0.5	L1	4186624	968	968	244	244
2MASS J14392836+1929149	L1	L1	4187136	976	976
2MASS J11083081+6830169	L1	...	4187648	968	968
2MASS J16580380+7027015	L1	...	4193024	968	968
Kelu-1AB	L2	L3 ± 1	4187904	976	976
2MASS J15065441+1321060	L3	...	12496384	976	976
2MASS J16154416+3559005	L3	...	4194048	968	968	976	976
2MASS J00361617+1821104	L3.5	L4 ± 1	4188672	484	484	488	976
2MASS J22244381-0158521	L4.5	L3.5	4189440	976	976
2MASS J15074769-1627386	L5	L5.5	4190208	976	976
SDSS J053951.99-005902.0	L5	L5	4190720	968	968
2MASS J12392727+5515371	L5	...	4194304	968	968
2MASS J15150083+4847416	L6.5	4190720	976	976
2MASS J17281150+3948593	L7	...	4191744	968	968
2MASS J15261405+2043414	L7	...	4191488	968	968
2MASS J08251968+2115521	L7.5	L6	4191232	968	968
DENIS-P J025503.3-470049.0	L8	L9	4192000	484	484	488	976
GI 584C	L8	...	1249776	3904	3904
2MASS J09293364+3429527	L8	...	4195072	968	968
GI 337CD	L8	T0	12494080	2928	2928
SDSS J042348.57-041403.5AB	L7.5	T0	12495360	976	976
SDSS J125453.90-012247.4	T2	T2	4185088	968	968
ε Ind Ba/Bb	T2.5	6313730	488	488	488	976
SDSS J102109.69-030420.1AB	T3	4183808	3904	3904
2MASS J05591914-1404488	T5	T4.5	4183296	968	968
...	4183040	976	976
2MASS J15031961+2525196	T6	T5.5	6314496	976	976
SDSS J162414.37+002915.6	T6	4185600	3904	3904
2MASS J12255432-2739466AB	T6	T6	12496128	976	976
2MASS J09373487+2931409	T7p	T6p	4195328	968	968
2MASS J12373919+6526148	T7	T6.5	4184832	968	968
2MASS J12171110-0311131	T7	T7.5	4184320	976	976
GI 570D	T7	T7.5	4186368	3904	3904

^a Spectral types of the M dwarfs are from Kirkpatrick et al. (1991, 1995), Henry et al. (1994), Hawley et al. (1996), Rebolo et al. (1998), and J. D. Kirkpatrick (2006, private communication). Spectral types of the L dwarfs are from Kirkpatrick et al. (1999, 2000, 2001), Fan et al. (2000), Reid et al. (2000), Gizis et al. (2000), Wilson et al. (2001, 2003), Cruz et al. (2003), Burgasser et al. (2006b), and Knapp et al. (2004). Spectral types of the T dwarfs are from Burgasser et al. (2003, 2006b), except for ε Ind Ba/Bb, which is from Scholz et al. (2003). Spectral types for binaries are derived from unresolved spectra. Errors on spectral types are ±0.5 subclass unless otherwise noted.

^b SL2 = Short-Low order 2, SL1 = Short-Low order 1, LL2 = Long-Low order 2, LL1 = Long-Low order 1.

^c Original target was GI 752B.

^d Original target was GJ 1001B.

0.77 to 1.5 with a median value of 0.97 and a median absolute deviation¹⁴ of 0.04.

¹⁴ The median absolute deviation is defined as $MAD = 1.4826 \times \text{median}\{|x_i - \text{median}(x)|\}$ and is a robust estimate of the standard deviation, σ , of a distribution. The constant of 1.4826 is defined such that $MAD = \sigma$ if the random variable x follows a normal distribution and the sample is large.

A subset of the M, L, and T dwarf SL spectra is shown in Figures 1–3. The signal-to-noise ratio (S/N) of the spectra ranges from several hundred for the early-type M dwarfs to a few for the faintest T dwarfs. Prominent absorption features of H₂O, CH₄, and NH₃ are indicated. Figure 4 shows the LL spectra of those dwarfs in our sample with the highest S/N. The S/N of the spectra ranges from >100 for GI 229A to a few for DENIS J0255–4700. The LL

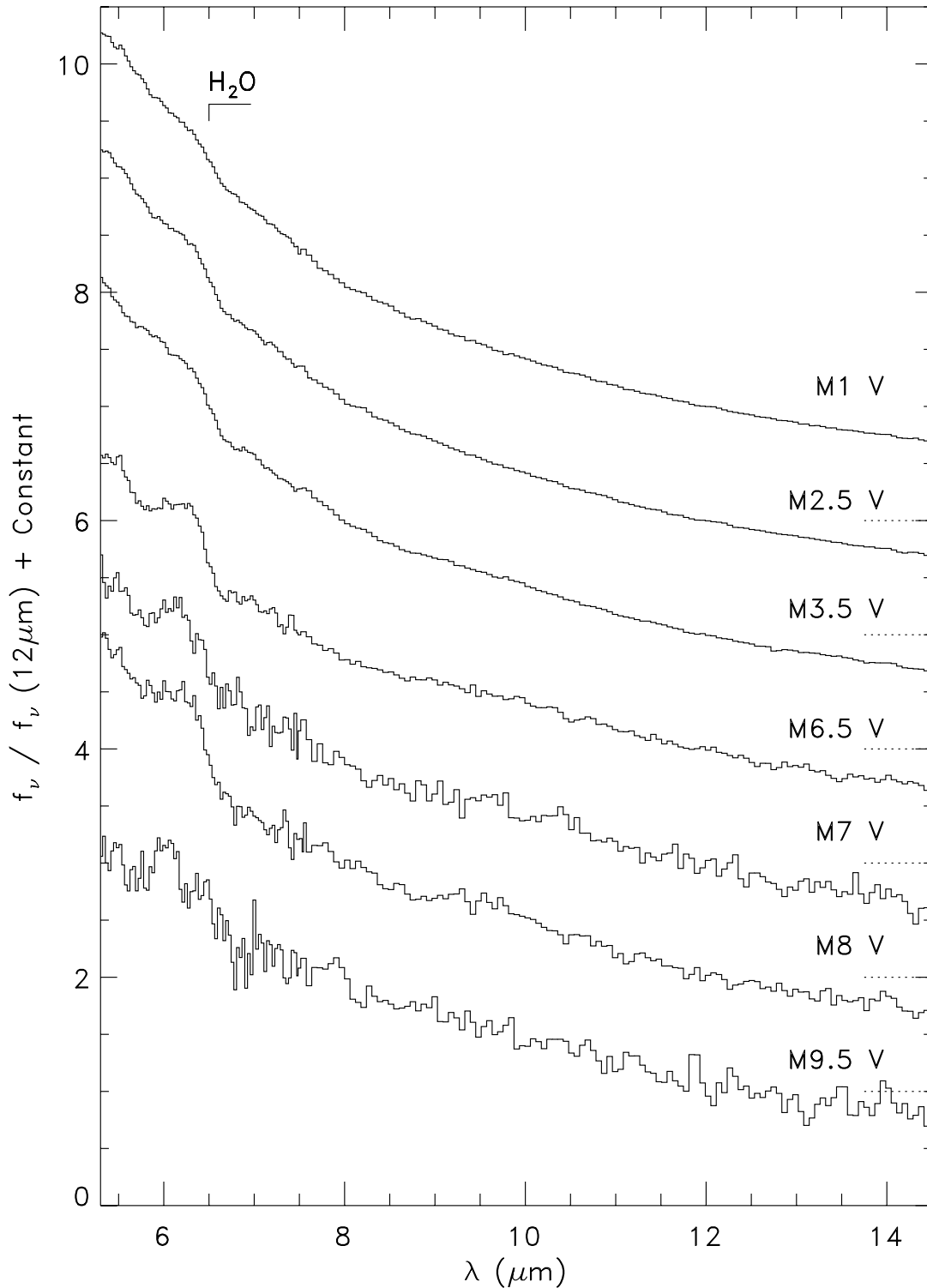


FIG. 1.—The 5.5–14.5 μm spectra of Gl 229A (M1 V), Gl 752A (M2.5 V), GJ 1001A (M3.5 V), GJ 1111 (M6.5 V), LHS 3003 (M7 V), vB 10 (M8 V), and BRI 0021–0214 (M9.5 V). The spectra have been normalized at 12 μm and offset by constants (*dotted lines*); the flux densities of the spectra at 12 μm are 872, 519, 36.4, 70.0, 15.4, 17.6, and 4.90 mJy, respectively.

spectra of ultracool dwarfs are relatively featureless at the resolving power of the IRS. Weck et al. (2004) found that the inclusion of the ground-state $\Delta\nu = +1$ bands of LiCl at $\sim 15.8 \mu\text{m}$ affects synthetic spectra at the level of a few percent at $T_{\text{eff}} = 1500 \text{ K}$ (the approximate T_{eff} of DENIS J0255–4700). Given the low S/N of the LL spectra, and the predicted weakness of the LiCl bands, we cannot assess whether this band is present in

the spectra of ultracool dwarfs. We do not discuss the LL spectra further.

3. DISCUSSION

To aid the reader in the interpretation of these spectra, a sequence of model spectra with values of T_{eff} ranging from 3800 K down to 600 K in steps of 400 K with a $\log g = 5.0$ is shown in

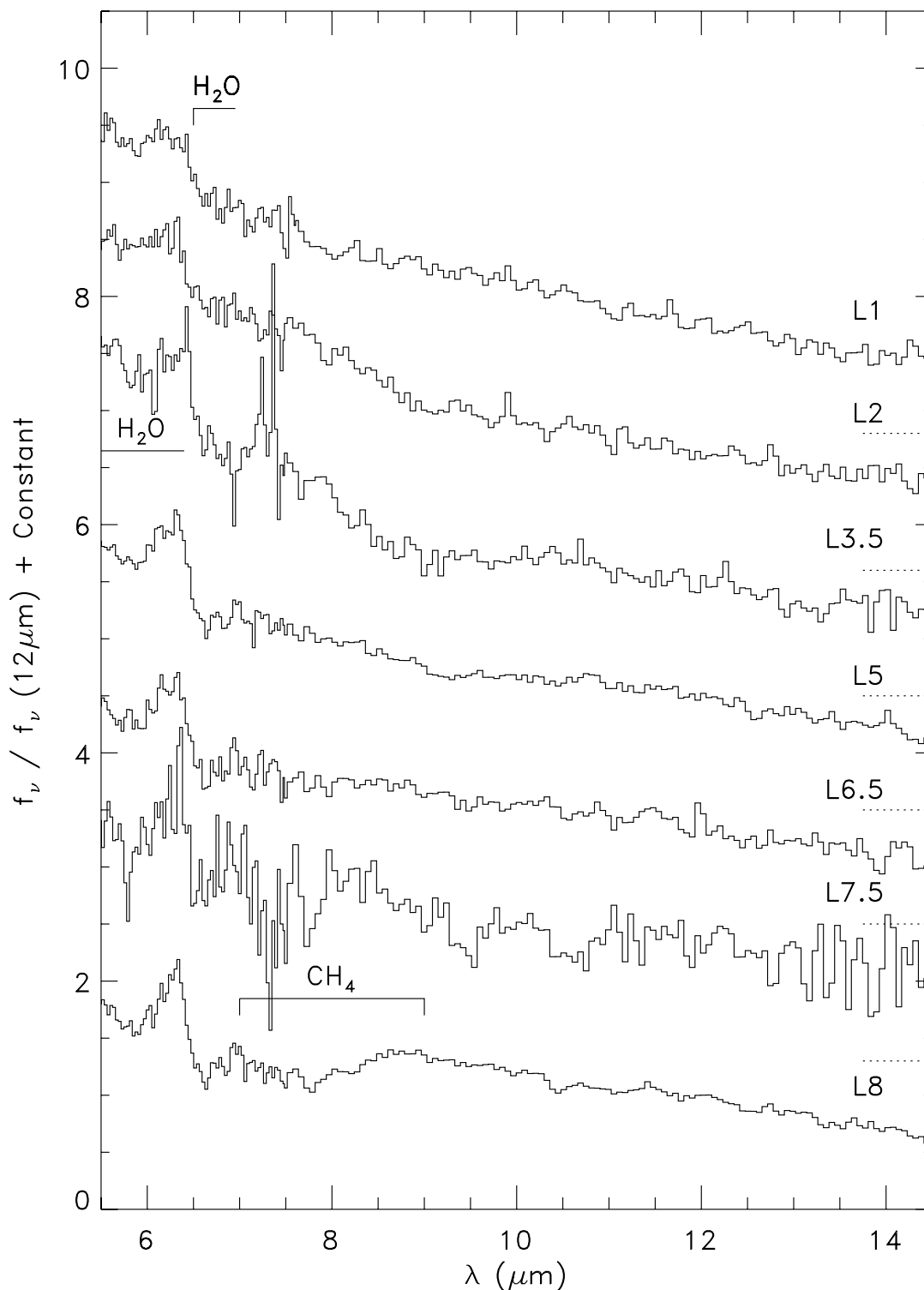


FIG. 2.—The 5.5–14.5 μm spectra of 2MASS J1439+1929 (L1), Kelu-1AB (L2), 2MASS J0036+1821 (L3.5), 2MASS J1507–1627 (L5), 2MASS J1515+4847 (L6.5), 2MASS J0825+2115 (L7.5), and DENIS J0255–4700 (L8). The spectra have been normalized at 12 μm and offset by constants (dotted lines); the flux densities of the spectra at 12 μm are 2.13, 2.00, 3.57, 4.47, 2.24, 2.00, and 7.14 mJy, respectively.

Figure 5. The models with $T_{\text{eff}} \geq 2600$ K are AMES-COND models (Allard et al. 2001), the models with $1400 \text{ K} \leq T_{\text{eff}} < 2600$ K are cloudy models (Marley et al. 2002; M. S. Marley et al. 2006, in preparation), and the models with $T_{\text{eff}} < 1400$ K are cloudless models. The spectra have been smoothed to $R = 90$ and resampled onto the wavelength grid of the IRS spectra. Also shown are the approximate spectral types corresponding to each T_{eff} (Leggett et al. 2000; Golimowski et al. 2004).

The spectra of the M and L dwarfs at $\lambda > 5 \mu\text{m}$ are dominated almost entirely by absorption features arising from the ν_2 fundamental band of H_2O centered at $\sim 6.27 \mu\text{m}$, and the $2\nu_2 - \nu_2$ overtone band centered at $\sim 6.42 \mu\text{m}$. However, due to a combination of the weakness of these features and the low spectral resolving power of the IRS spectra ($R \approx 90$), the only H_2O feature readily identifiable is a “break” at $\sim 6.5 \mu\text{m}$. As the T_{eff} decreases, this break generally increases in strength until eventually

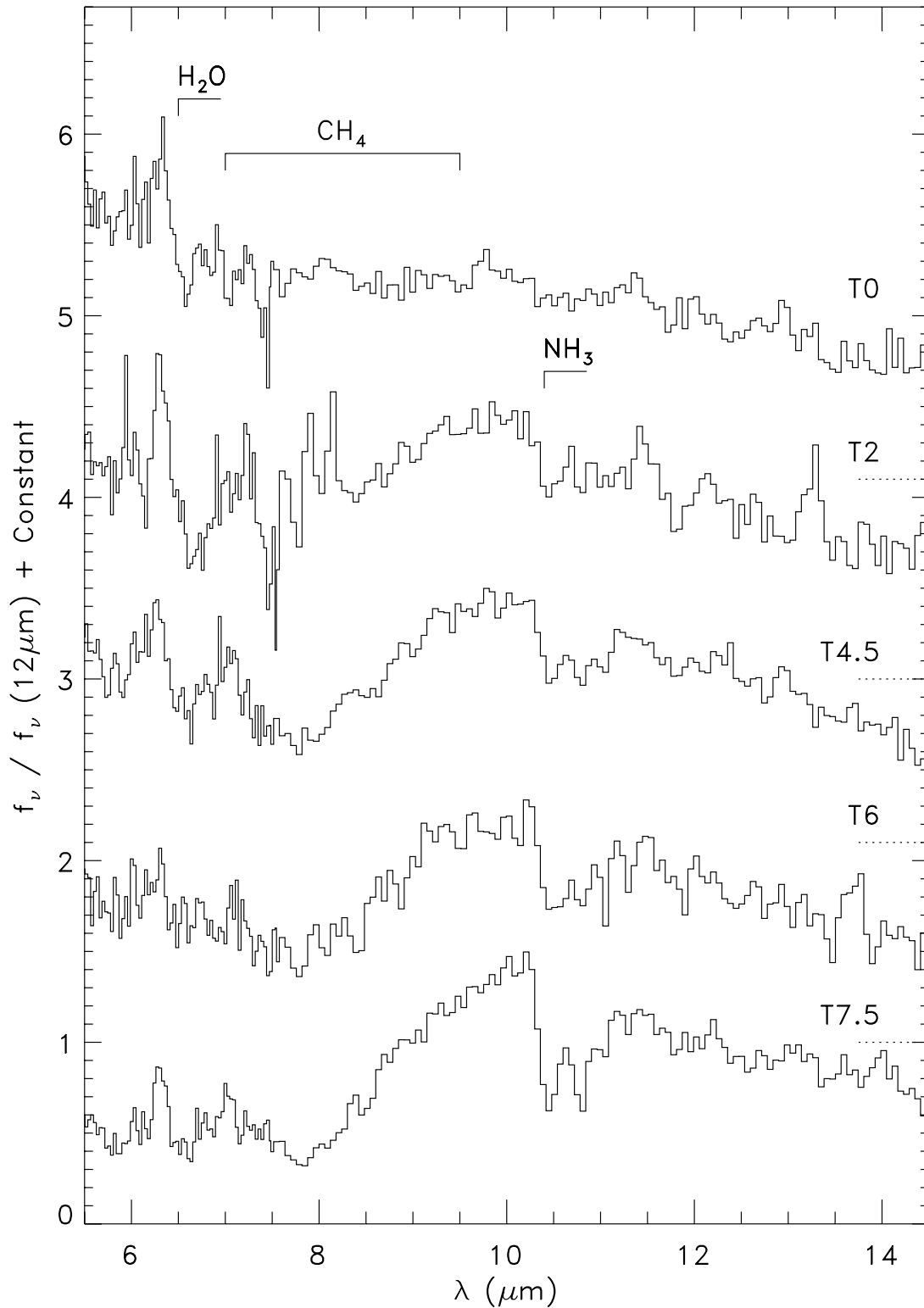


FIG. 3.—The 5.5–14.5 μm spectra of SDSS J0423–0414AB (T0), SDSS J1254–0122 (T2), 2MASS J0559–1404 (T4.5), SDSS J1624+0029 (T6), and Gl 570D (T7.5). The spectra have been normalized at 12 μm and offset by constants (dotted lines); the flux densities of the spectra at 12 μm are 2.27, 1.40, 2.10, 0.775, and 1.82 mJy, respectively.

additional H_2O absorption at longer and shorter wavelengths transforms it into an emission-like feature in the spectra of the T dwarfs. In actuality, this emission feature is a result of a minimum in the H_2O opacity, which allows the observer to see deeper, and thus hotter, atmospheric layers. Counterintuitively, the $T_{\text{eff}} = 2600$ K COND model ($\sim\text{M7 V}$) shows stronger H_2O

absorption from 8 to 10 μm (P. Hauschildt 2005, private communication) than the $T_{\text{eff}} = 2200$ K cloudy model ($\sim\text{L1}$). As can be seen in Figures 1 and 2, we see no evidence of this absorption in the spectra of the late-type M and early-type L dwarfs. The ν_4 fundamental band of CH_4 centered at ~ 7.65 μm first appears in the spectra of the latest L dwarfs ($T_{\text{eff}} \approx 1500$ K) and

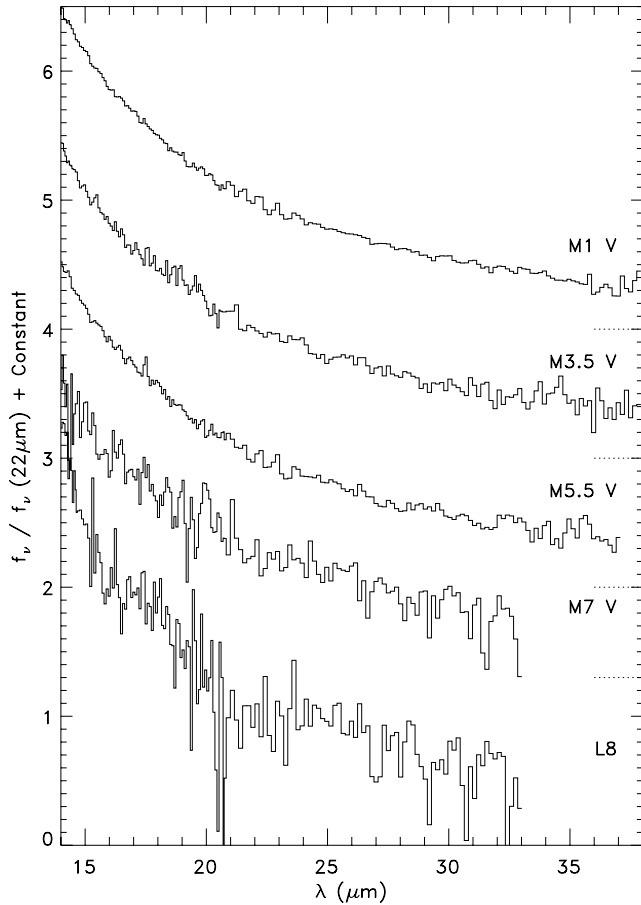


FIG. 4.—The 15–38 μm spectra of Gl 229A (M1 V), GJ 1001A (M3.5 V), Gl 65AB (M5.5 V), LHS 3003 (M7 V), and DENIS J0255–4700 (L8). The spectra have been normalized at 22 μm and offset by constants (dotted lines); the flux densities at 22 μm are 242, 11.5, 91.0, 4.87, and 1.57 mJy, respectively. The longest wavelengths have been removed from some of the spectra due to a low S/N.

grows in strength through the T sequence. The combination of H_2O and CH_4 absorption from roughly 4 to 9 μm heavily suppresses the flux at these wavelengths in the spectra of the T dwarfs. Finally, the ν_2 fundamental band of NH_3 centered at ~ 10.5 μm appears in the spectra of the early- to mid-type T dwarfs. The only clearly discernible NH_3 feature is the double Q-branch feature centered at 10.5 μm ; the double Q-branch is a result of inversion doubling (Herzberg 1945). Overall, the theoretical spectra provide a reasonably good match to the mid-infrared spectra of M, L, and T dwarfs. A more detailed comparison between the models and the observations is currently in progress (M. C. Cushing et al. 2006, in preparation).

We have defined three spectral indices that measure the depths of the H_2O bands at ~ 6.3 μm , the 7.65 μm CH_4 band, and the 10.5 μm NH_3 band in the IRS spectra of the M, L, and T dwarfs. Figure 6 shows an illustration of the three spectral indices along with the spectrum of 2MASS J0559–1404 (T4.5). As described above, the only H_2O feature readily identifiable in the IRS spectra of ultracool dwarfs is located at ~ 6.5 μm . We have therefore defined an index that measures the amplitude of the 6.25 μm peak relative to the two minima on either side. This index is given by

$$\text{IRS H}_2\text{O} = \frac{f_{6.25}}{0.562f_{5.80} + 0.474f_{6.75}}, \quad (5)$$

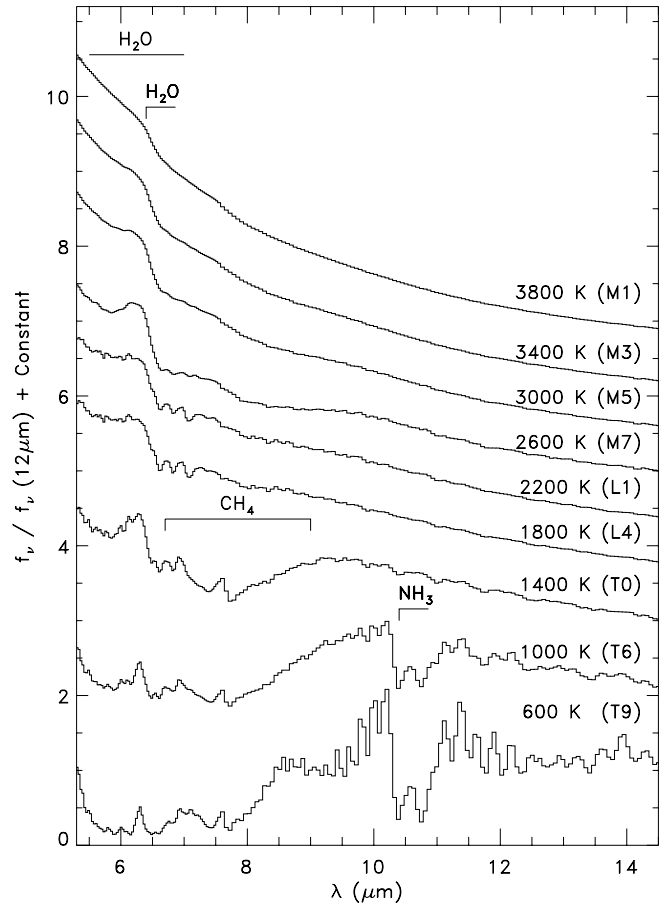


FIG. 5.—Model sequence from $T_{\text{eff}} = 3800$ to 600 K, in steps of 400 K. The models with $T_{\text{eff}} \geq 2600$ K are AMES-COND models (Allard et al. 2001), the models with $1400 \text{ K} \leq T_{\text{eff}} < 2600$ K are cloudy models (Marley et al. 2002; M. S. Marley et al. 2006, in preparation), and the models with $T_{\text{eff}} < 1400$ K are cloudless models. The spectra have been smoothed to $R = 90$ and resampled onto the wavelength grid of the IRS spectra. The approximate spectral types corresponding to the effective temperatures are from Leggett et al. (2000) and Golimowski et al. (2004).

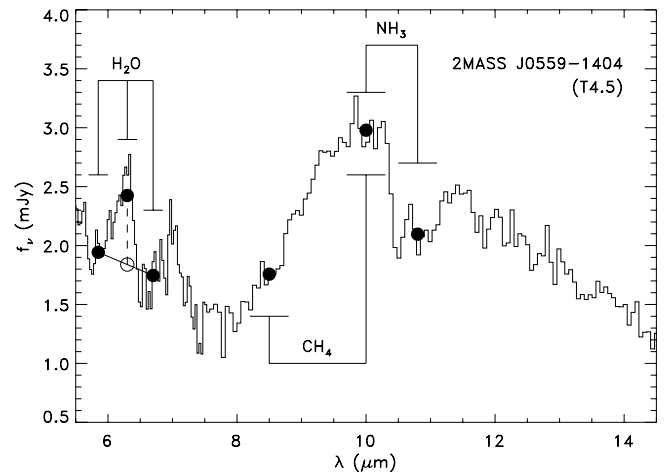


FIG. 6.—Illustration of the H_2O , CH_4 , and NH_3 spectral indices with the spectrum of 2MASS J0559–1404 (T4.5).

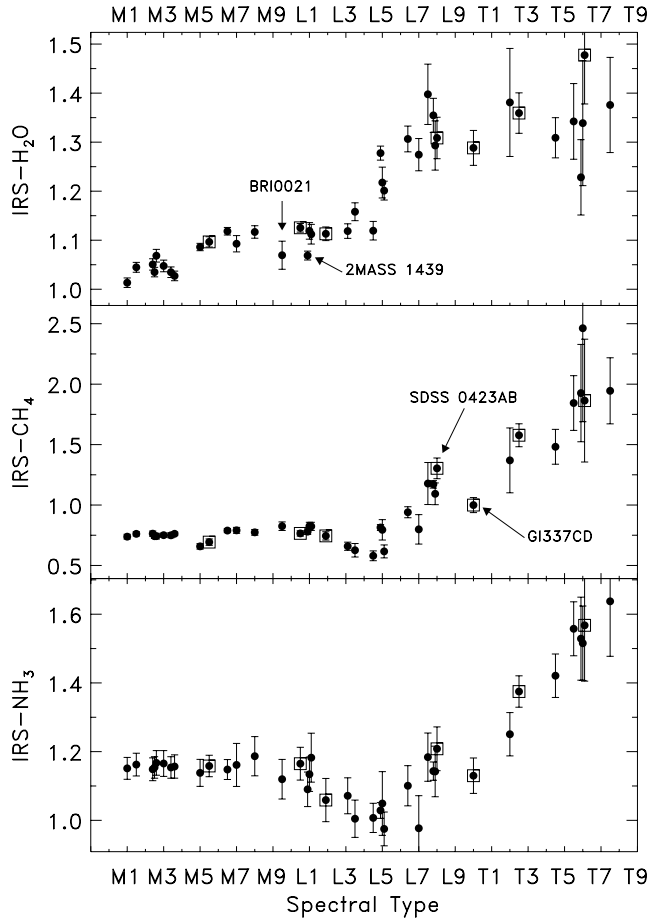


FIG. 7.—IRS H₂O, IRS CH₄, and IRS NH₃ spectral indices of the dwarfs in our sample, as a function of spectral type. Individual objects discussed in the text are indicated, and known binaries are marked with open squares.

where f_{λ_0} is the mean flux density in a $0.15 \mu\text{m}$ window centered around λ_0 . Both the CH₄ and NH₃ indices are simple ratios of the flux density in and out of an absorption feature and are defined as

$$\text{IRS CH}_4 = \frac{f_{10.0}}{f_{8.5}} \quad (6)$$

$$\text{IRS NH}_3 = \frac{f_{10.0}}{f_{10.8}}, \quad (7)$$

where f_{λ_0} is the mean flux density in a $0.3 \mu\text{m}$ window centered around λ_0 . The values of the indices computed for the dwarfs in our sample are shown as a function of spectral type in Figure 7. The errors were computed from the uncertainties in the mean flux densities f_{λ_0} . Larger values of a given index imply stronger absorption.

The IRS H₂O values indicate that, overall, the H₂O absorption-band strength increases with increasing spectral type until it saturates in the T spectral class. Nevertheless, there also appears to be a plateau from about $\sim\text{M7 V}$ to $\sim\text{L5}$, indicating that late-type M dwarfs and early- to mid-type L dwarfs have similar H₂O band strengths. BRI 0021–0214 (M9.5 V) and 2MASS J1439+1929 (L1) appear to have anomalously low H₂O band strengths. The variations of the IRS CH₄ and IRS NH₃ values with spectral type are, in contrast, much simpler. The onset of CH₄ absorption occurs at roughly the L/T transition. A more precise spectral type cannot be assigned, given the coarse wavelength sampling, low resolving power, and moderate S/N of the IRS spectra. It is interesting to

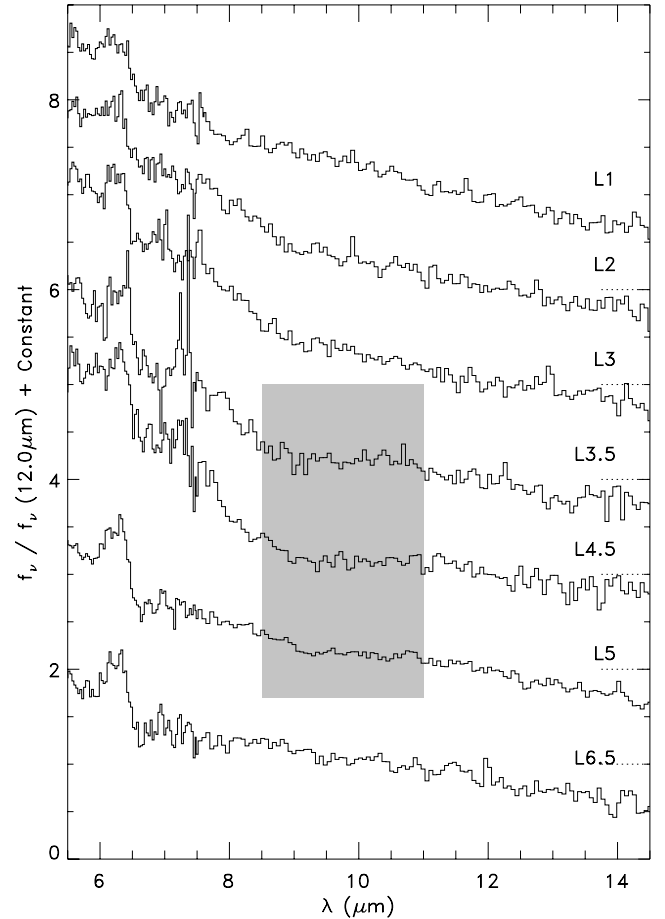


FIG. 8.—IRS spectra of 2MASS J1439+1929 (L1), Kelu-1AB (L2), 2MASS J1506+1321 (L3), 2MASS J0036+1821 (L3.5), 2MASS J2224–0158 (L4.5), 2MASS J1507–1627 (L5), and 2MASS J1515+4847 (L6.5). The spectra have been normalized at $12 \mu\text{m}$ and offset by constants (dotted lines); the flux densities of the spectra at $12 \mu\text{m}$ are 2.13, 2.00, 1.94, 3.57, 1.64, 4.47, and 2.24 mJy, respectively. The gray box indicates the wavelength range ($9\text{--}11 \mu\text{m}$) and objects that exhibit the plateau.

note that the ν_3 fundamental band of CH₄ at $3.3 \mu\text{m}$ has been detected in the spectra of mid-type L dwarfs (Oppenheimer et al. 1998; Burgasser 2001; Noll et al. 2000; Cushing et al. 2005). The absorption cross section of the ν_4 band of CH₄ centered at $7.65 \mu\text{m}$ is roughly an order of magnitude smaller than that of the ν_3 band ($T = 1000 \text{ K}$, $P = 1 \text{ bar}$; R. Freedman 2005, private communication), so it is not surprising that the ν_4 band appears later in the spectral sequence than the ν_3 band. Finally, The IRS NH₃ values also indicate that the onset of NH₃ absorption also occurs near the L/T transition. It is interesting to note that the values of both the IRS CH₄ and IRS NH₃ indices decrease through the L spectral class, a behavior we discuss in § 3.1.1.

3.1. Objects of Interest

As described above, the mid-infrared spectral features of M, L, and T dwarfs generally show a smooth variation with spectral type and are qualitatively well matched by model spectra. However, there are a number of interesting objects that stand out against this sequence, which we discuss in the following subsections.

3.1.1. Mid-Type L Dwarfs

It has been apparent for some time that the atmospheres of L dwarfs are cloudy. The formation of these condensate (i.e., dust) clouds in the atmospheres of ultracool dwarfs has a dramatic

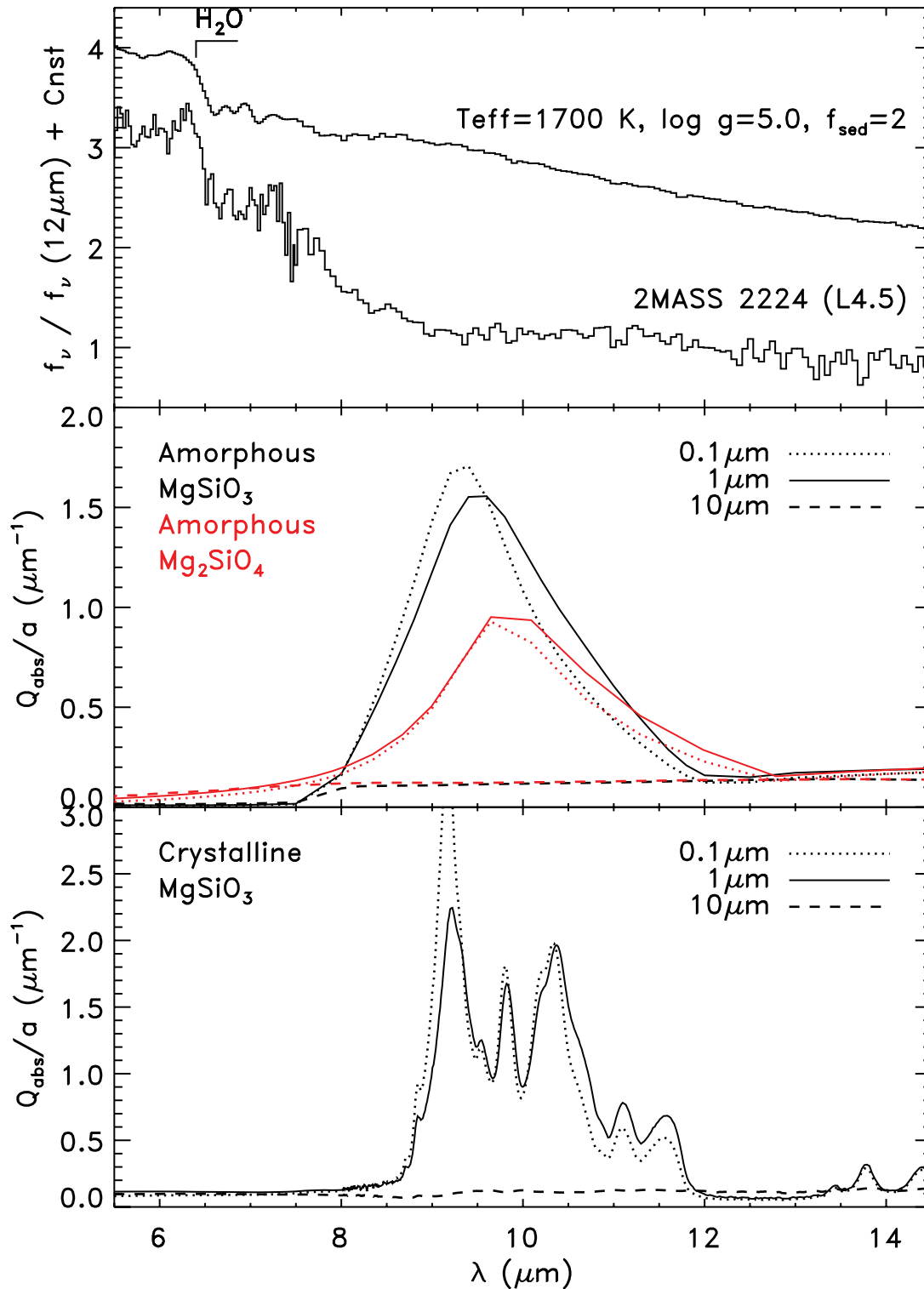


FIG. 9.—*Top*: Spectrum of 2MASS J2224–0158 (L4.5) and a model ($T_{\text{eff}} = 1900 \text{ K}$, $\log g = 5.0$, $f_{\text{sed}} = 2$) appropriate for an L4.5 dwarf, from M. S. Marley et al. (2006, in preparation). *Middle*: Optical absorption (Q_{abs}/a) for amorphous enstatite (MgSiO_3 ; black) and forsterite (Mg_2SiO_4 ; red) for three different particle sizes: $0.1 \mu\text{m}$ (dotted lines), $1 \mu\text{m}$ (solid lines), and $10 \mu\text{m}$ (dashed lines). *Bottom*: Optical absorption (Q_{abs}/a) for crystalline enstatite (MgSiO_3) for three different particle sizes: $0.1 \mu\text{m}$ (dotted lines), $1 \mu\text{m}$ (solid lines), and $10 \mu\text{m}$ (dashed lines).

impact on their atmospheric structure (T/P profile) and thus their emergent spectra. Models that neglect dust formation produce near-infrared colors that are much bluer than the observations (Allard et al. 2001; Marley et al. 2002; Knapp et al. 2004; Burrows et al. 2006). However, the limited wavelength span of near-infrared spectra has precluded definitive determinations of

either particle size or condensate composition. IRS spectra both substantially increase the wavelength range of L dwarf spectra—allowing for Mie scattering effects to be constrained—and cover the location of the $10 \mu\text{m}$ silicate feature.

While the IRS spectra of the early-type L dwarfs and the T dwarfs are in generally good agreement with the model predictions

(Roellig et al. 2004; M. C. Cushing et al. 2006, in preparation), the spectra of mid- to late-type L dwarfs differ substantially from the models. Figure 8 shows a sequence of L dwarfs with spectral types ranging from L1 to L6.5. As can be seen, the spectrum of 2MASS J2224–0158 (L4.5) exhibits a prominent plateau from roughly 9 to 11 μm . A similar, although weaker, plateau can also be seen in the spectra of 2MASS J0036+1821 (L3.5) and 2MASS J1507–1627 (L5). This feature is also clearly absent in the spectra of L dwarfs with both earlier and later spectral types. This plateau is the cause of the decreasing IRS CH₄ and IRS NH₃ values in the L dwarfs (see § 3), since these indices are also a measure of the overall spectral slope in the M and L dwarf spectra. The broad deviation of the model from the observed spectra implies that the model is missing or incorrectly characterizing a continuum opacity source. Given the good agreement between model and data at early and late spectral types, a missing gaseous opacity source with a smooth continuum seems unlikely. We thus conclude that the most likely explanation for the deviation is the description of the cloud opacity.

The IRS spectral region of course includes the 10 μm silicate feature that arises from the Si–O stretching vibration in silicate grains. The spectral shape and importance of the silicate feature depend on the particle size and composition of the silicate grains. In BD atmospheres the first expected silicate condensate is forsterite, Mg₂SiO₄ (Lodders 2002), at $T \approx 1700$ K ($P = 1$ bar).¹⁵ Since Mg and Si have approximately equal abundances in a solar composition atmosphere, the condensation of forsterite leaves substantial silicon, present as SiO, in the gas phase. In equilibrium, at temperatures about 50 to 100 K cooler than the forsterite condensation temperature, the gaseous SiO reacts with the forsterite to form enstatite, MgSiO₃ (Lodders 2002). Since the precise vertical distribution of silicate species depends on the interplay of the atmospheric dynamics and chemistry, the models (M. S. Marley et al. 2006, in preparation) do not attempt to capture those details. Instead, all of the silicate condensates are assumed to be forsterite—since it condenses first—and the optical properties of forsterite are employed in the calculation of the Mie absorption and scattering efficiencies.

In addition to composition, the cloud spectral properties are sensitive to particle size. There is likely a range of particle sizes ranging from very small, recently condensed grains, to larger grains that have grown by accumulation (Ackerman & Marley 2001; Woitke & Helling 2004). The atmosphere model includes a calculation of turbulent diffusion and particle sedimentation to compute a mean particle size (Ackerman & Marley 2001), assuming a log-normal size distribution with fixed width $\sigma = 2$. The Ackerman & Marley cloud model predicts submicron particle sizes high above the condensation layer (as do Woitke & Helling 2004), but these small particles do not provide enough opacity to produce a detectable effect on the model spectra. In the optically thick cloud the model predicts mean particle sizes of 5–10 μm and larger. Such a population of particles is too large to produce a 10 μm silicate feature.

Figure 9 compares the absorption efficiency of silicate grains of various sizes, composition, and crystal structures to the spectrum of 2MASS J2224–0158 (L4.5). For each species the quantity Q_{abs}/a , or Mie absorption efficiency divided by particle radius, is shown. This is the relevant quantity, since, all else being equal, the total cloud absorption optical depth is proportional to this quantity (Marley 2000). The middle panel of Figure 9 leads us to conclude that the mismatch between the models and data may arise from a

population of silicate grains that is not captured by the cloud model. The large grain sizes computed by the cloud model (~ 10 μm) tend to have relatively flat absorption spectra (*dashed lines*) across the IRS spectral range. Only grains smaller than about 2 μm in radius show the classic 10 μm silicate feature (Hanner et al. 1994), which suggests that the cloud model does not produce enough small grains. In addition, the combined width of the enstatite, whose opacity is currently not included in the atmosphere models, and forsterite features is a better match to the width of the plateau in the spectrum of 2MASS J2224–0158.

Furthermore, the model employs amorphous silicate optical properties. It is possible, especially at the higher pressures found in BD atmospheres, that the grains are crystalline, not amorphous. Indeed, laboratory solar-composition condensation experiments at relevant pressures produce crystalline, not amorphous, silicates (Toppani et al. 2004). Crystalline grains (Fig. 9, *bottom panel*) can have larger and spectrally richer absorption cross sections. The strongest absorption feature of crystalline enstatite in the IRS wavelength range occurs at ~ 9.17 μm . The weak absorption feature in the IRS spectrum of 2MASS J1507–1627 (L5; see Fig. 8) at the same wavelength may therefore be carried by crystalline enstatite. However, higher S/N spectra would be required to confirm this tentative identification.

Finally, we note that Helling et al. (2006) predicted that non-equilibrium effects will lead to the condensation of quartz (SiO₂) grains within the silicate cloud. Quartz absorption begins somewhat bluer than that of enstatite and, given small enough particle sizes, also might add to the spectral flattening seen in Figures 8 and 9. Along with IRS observations of more mid-type L dwarfs, detailed cloud modeling considering a range of cloud sizes and compositions will be required to fully constrain the particular species, particle sizes, and crystallinity present in the silicate cloud.

3.1.2. *Gl 337CD and SDSS J0423–0414AB*

Gl 337CD was discovered by Wilson et al. (2001) and later resolved into a near-equal-magnitude (K_s flux ratio of 0.93 ± 0.10) binary separated by $0''.53$ by Burgasser et al. (2005a). Its unresolved near-infrared spectrum exhibits weak CH₄ absorption (McLean et al. 2003), resulting in a near-infrared spectral type of T0 (Burgasser et al. 2006b), while its unresolved red-optical spectrum has been typed as L8 (Wilson et al. 2001). The absolute K_s magnitudes of the components provide little constraint on the individual spectral types of the two objects, since the M_{K_s} values are consistent with a broad range of types from late-type L dwarfs through mid-type T dwarfs. Given the composite optical and near-infrared spectral types of L8 and T0, respectively, the pair is likely composed of a late-type L and early- to mid-type T dwarf. SDSS J0423–0414AB (hereafter SDSS 0423AB) was discovered by Geballe et al. (2002) and subsequently resolved into a binary separated by $0''.16$ by Burgasser et al. (2005b). It was also classified as T0 based on the presence of weak CH₄ absorption in its near-infrared spectrum (Geballe et al. 2002; Burgasser et al. 2006b) and has an unresolved optical spectral type of L7.5 (Cruz et al. 2003; J. D. Kirkpatrick 2006, in preparation). Burgasser et al. (2005b) found that a hybrid spectrum composed of an L6.5 and T2 dwarf provides an excellent match to the unresolved near-infrared spectrum of SDSS 0423AB.

Figure 10 shows the IRS spectra of SDSS 0423AB and Gl 337CD. Although the spectra have almost identical (unresolved) optical and near-infrared spectral types, their mid-infrared spectra look markedly different. In particular, the CH₄ band centered at 7.65 μm is much stronger in the spectrum of Gl 337CD (see also Fig. 7). Also shown are composite L5+T2 and L8+T4.5 spectra

¹⁵ Iron-bearing species [e.g., olivine, (Mg,Fe)₂SiO₄] are not expected, since iron condenses well before the first silicate.

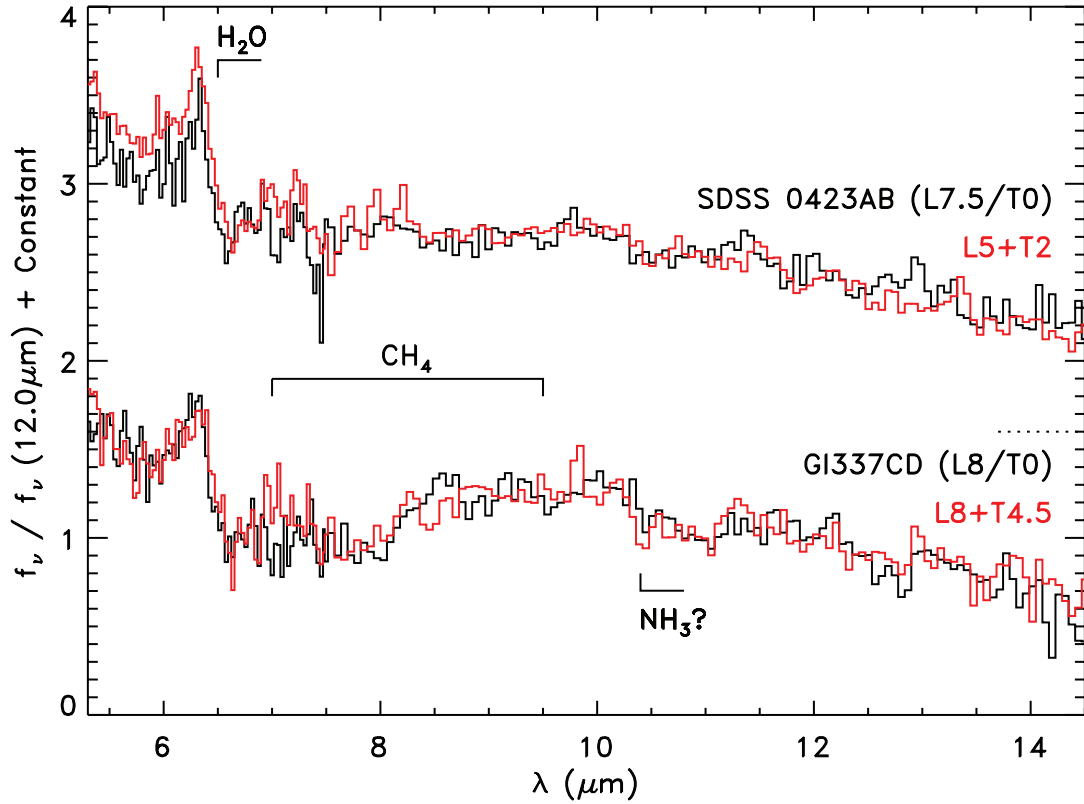


FIG. 10.—IRS spectra of SDSS 0423–0414AB and G1 337CD (*black lines*). Their unresolved optical/near-infrared spectral types are L7.5/T0 and L8/T0, respectively. Also shown are composite L5+T2 and L8+T4.5 spectra (*red*) constructed from the spectra of 2MASS J1507–1627 (L5), SDSS J1254–0122 (T2), G1 584C (L8), and 2MASS J0559–1404 (T4.5). The spectra have been normalized to unity at 12 μm and offset by constants (*dotted lines*).

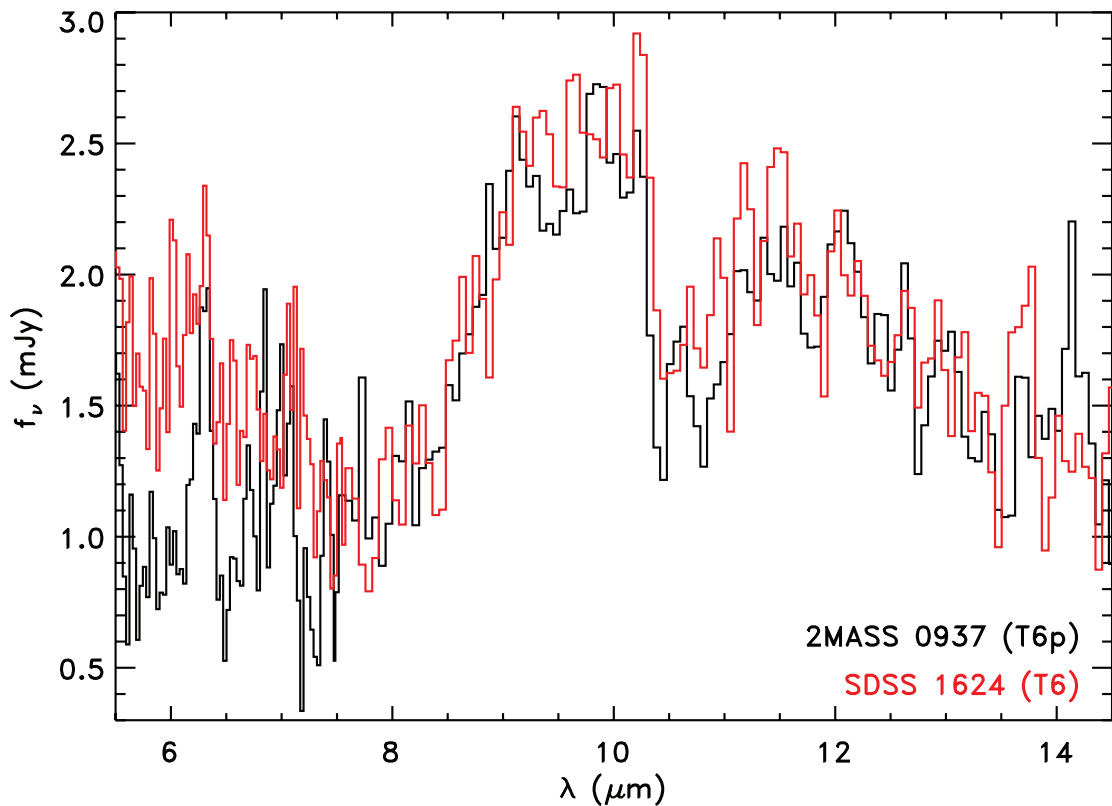


FIG. 11.—IRS spectra of 2MASS J0937+2931 (T6p; *black*) and 2MASS SDSS J1264+0029 (T6; *red*). The spectrum of SDSS J1264+0029 has been scaled by the ratio of the distances of the two objects to adjust its flux to the level that would be observed if it were at the distance of 2MASS J0937+2931. The spectrum of SDSS J1264+0029 differs significantly from that of 2MASS J0937+2931 at $\lambda \lesssim 7.5 \mu\text{m}$.

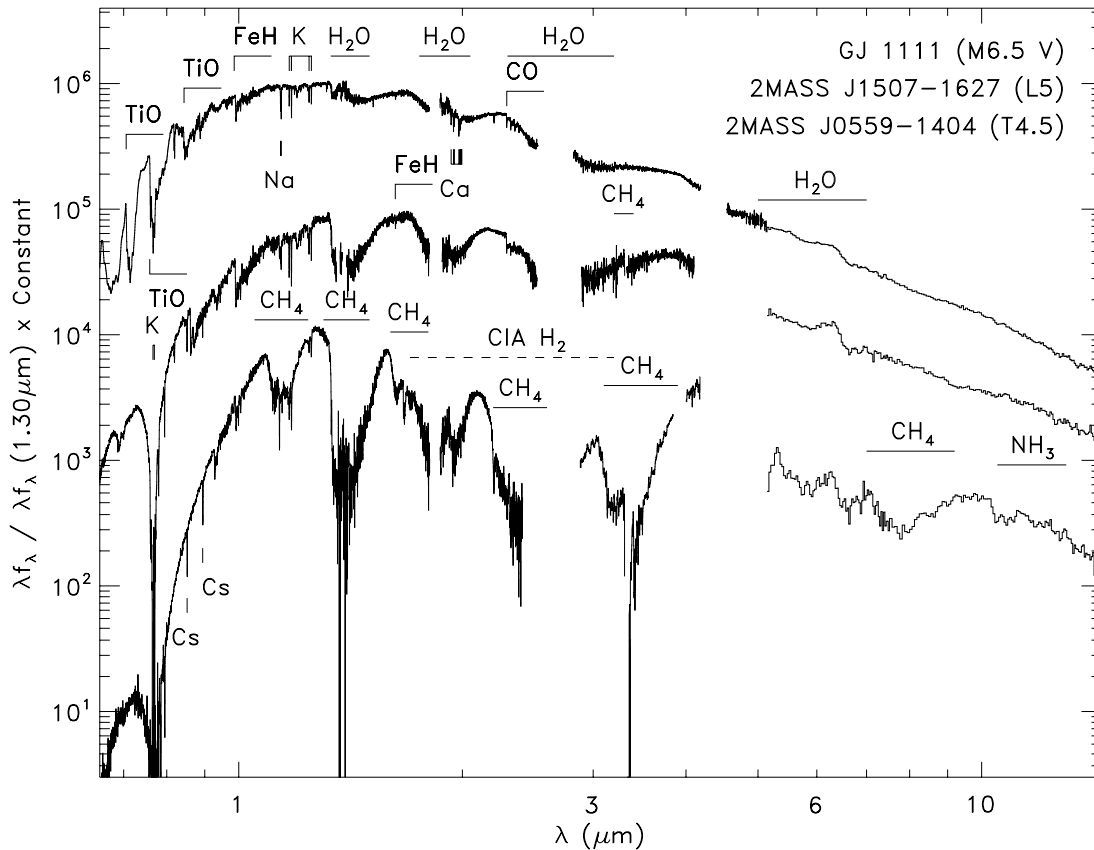


FIG. 12.—The 0.65–14.5 spectra of GJ 1111 (M6.5 V), 2MASS J1507–1627 (L5), and 2MASS J0559–1404 (T4.5). The red-optical spectra are from Kirkpatrick et al. (1991), Reid et al. (2000), and Burgasser et al. (2003), and the near-infrared spectra are from Cushing et al. (2005) and J. T. Rayner et al. (2006, in preparation). Note that the flux density units are λf_λ . The spectra have been normalized to unity at $1.3 \mu\text{m}$ and multiplied by constants. The CIA H_2 absorption is indicated as a dashed line because it shows no distinct spectral features but rather a broad, smooth absorption.

(red lines) constructed after scaling the spectra of 2MASS J1507–1627 (L5), SDSS J1254–0122 (T2), DENIS J0255–4700 (L8), and 2MASS J0559–1404 (T4.5) to appear as if they were at a common distance. Although Burgasser et al. (2005b) found that an L6.5+T2 composite near-infrared spectrum was the best match to that of SDSS 0423AB, we used an L5 dwarf, since our sample lacks an L6 dwarf with a measured trigonometric parallax. Nevertheless, the agreement between the data and composite spectra is quite good. The weak CH_4 band in SDSS 0423AB is therefore a result of the intrinsically brighter L6.5 dwarf, which lacks CH_4 absorption, veiling the CH_4 band in the spectrum of the T2 dwarf. In contrast, both components of GI 337CD (L8, T4.5) exhibit CH_4 absorption resulting in a prominent CH_4 band in its unresolved spectrum.

3.1.3. 2MASS J0937+2931

2MASS J0937+2931 (hereafter 2MASS 0937) is the archetypal peculiar T dwarf. It is classified as a T6p (Burgasser et al. 2006b) because it exhibits a number of spectral peculiarities, including an enhanced emission peak at $1.05 \mu\text{m}$, weak J -band K I lines, and a heavily suppressed K -band spectrum (Burgasser et al. 2002; Knapp et al. 2004). All of these spectral features are indicative of high-pressure (high surface gravity) and/or low-metallicity atmospheres. In particular, the suppression of the K band is a result of collision-induced H_2 1–0 dipole absorption (CIA H_2) centered at $2.4 \mu\text{m}$ (Borysow 2002; Knapp et al. 2004), which is enhanced in such environments. Indeed, Burgasser et al. (2006a) have shown that a synthetic spectrum with a moderately low metallicity ($-0.1 \leq [\text{M}/\text{H}] \leq -0.4$) and high surface grav-

ity ($5.0 \leq \log g \leq 5.5$) is required to adequately fit its 0.7 – $2.5 \mu\text{m}$ spectrum.

Figure 11 shows the IRS spectrum of 2MASS 0937 along with the spectrum of SDSS J1624+0029 (T6; hereafter SDSS 1624). The spectrum of SDSS 1624 has been scaled by the ratio of the distances of the two objects to adjust its flux to the level that would be observed if it were at the distance of 2MASS 0937. The spectrum of 2MASS 0937 appears significantly depressed shortward of $\sim 7.5 \mu\text{m}$ relative to the spectrum of SDSS 1624. Although we tentatively ascribe this behavior to the subsolar metallicity / high surface gravity of 2MASS 0937, we caution that additional high S/N IRS observations of late-type T dwarfs will be required to confirm that the mid-infrared spectrum of 2MASS 0937 is truly distinct from typical T dwarfs.

4. SPECTRAL ENERGY DISTRIBUTIONS AND BOLOMETRIC FLUXES

4.1. Spectral Energy Distributions

Figure 12 shows the 0.6 – $14.5 \mu\text{m}$ spectra of GJ 1111 (M6.5 V), 2MASS J1507–1627 (L5), and 2MASS J0559–1404 (T4.5). The red-optical spectra are from Kirkpatrick et al. (1991), Fan et al. (2000), and Burgasser et al. (2003), and the near-infrared spectra are from Cushing et al. (2005) and J. T. Rayner et al. (2006, in preparation). The changes in the spectral morphology across the MLT sequence illustrate all of the major chemical transitions expected to occur in the atmospheres of ultracool dwarfs (Fegley & Lodders 1996; Lodders 1999; Burrows & Sharp 1999; Lodders & Fegley 2002).

TABLE 2
BOLOMETRIC MAGNITUDES

OBJECT	OPTICAL SPECTRAL TYPE ^a	INFRARED SPECTRAL TYPE ^a	π^b (mas)	M_{bol}^c	
				Golimowski et al.	This Work
GI 229A	M1 V	...	173.17 ± 1.10	7.97 ± 0.09	7.92 ± 0.04
BRI 0021-0214	M9.5 V	...	84.2 ± 2.6	13.37 ± 0.10	13.45 ± 0.08
2MASS J07464256+2000321AB.....	L0.5	L1	81.9 ± 0.3	13.26 ± 0.07	13.29 ± 0.04
2MASS J14392836+1929149.....	L1	L1	69.6 ± 0.5	13.88 ± 0.07	14.01 ± 0.04
Kelu-1AB.....	L2	L3 \pm 1	53.6 ± 2.0	13.74 ± 0.11	13.78 ± 0.11
2MASS J00361617+1821104.....	L3.5	L4 \pm 1	114.2 ± 0.8	14.67 ± 0.07	14.64 ± 0.04
2MASS J22244381-0158521.....	L4.5	L3.5 \pm 1	87.02 ± 0.89	15.14 ± 0.07	15.16 ± 0.04
2MASS J1507476-162738.....	L5	L5.5	136.4 ± 0.6	15.16 ± 0.07	15.28 ± 0.04
SDSS J053951.99-005902.0.....	L5	L5	76.12 ± 2.17	15.12 ± 0.09	15.21 ± 0.07
2MASS J08251968+2115521.....	L7.5	L6	94.22 ± 0.99	16.10 ± 0.07	16.13 ± 0.04
SDSS J125453.90-012247.4.....	T2	T2	73.96 ± 1.59	16.08 ± 0.10	16.22 ± 0.06
2MASS J05591914-1404488.....	T5	T4.5	96.73 ± 0.96	16.07 ± 0.13	16.17 ± 0.04

^a Spectral types of the M dwarfs are from Kirkpatrick et al. (1991, 1995), Henry et al. (1994), Hawley et al. (1996), Rebolo et al. (1998), and J. D. Kirkpatrick (2006, private communication). Spectral types of the L dwarfs are from Kirkpatrick et al. (1999, 2000, 2001), Fan et al. (2000), Reid et al. (2000), Gizis et al. (2000), Wilson et al. (2001), Cruz et al. (2003), Burgasser et al. (2006b), and Knapp et al. (2004). The spectral types of the T dwarfs are from Burgasser et al. (2003, 2006b), except for the spectral type of ϵ Ind Ba/Bb, which is from Scholz et al. (2003). Spectral types for binaries are derived from unresolved spectra. Errors on spectral types are ± 0.5 subclass unless otherwise noted.

^b The trigonometric parallaxes are from Golimowski et al. (2004) and were taken from van Altena et al. (1995), Perryman et al. (1997), Tinney et al. (1995, 2003), Dahn et al. (2002), and Vrba et al. (2004).

^c $M_{\text{bol}} = -2.5 \log f_{\text{bol}} + 5 \log \pi - 13.978$, assuming $L_{\odot} = 3.86 \times 10^{26}$ W and $M_{\text{bol},\odot} = +4.75$.

In the atmospheres of M dwarfs ($2400 \text{ K} \lesssim T_{\text{eff}} \lesssim 3800 \text{ K}$), C, N, and O are found primarily in CO, N₂, and H₂O. The spectral morphology of M dwarfs is therefore shaped primarily by H₂O absorption bands, although TiO and VO bands dominate in the optical. The $\Delta\nu = +2$ CO bands at $\lambda \gtrsim 2.29 \mu\text{m}$ and absorption lines of refractory species such as Al, Mg, Fe, and Ca are also weakly present. Since N₂ is a homonuclear molecule, it cannot radiate in the dipole approximation and therefore shows no detectable spectral signatures in the spectra of M and L dwarfs (although N₂ can in principle absorb via collisions with H₂ molecules, akin to the CIA H₂ opacity [Borysow & Frommhold 1986]).

As T_{eff} approaches 2400 K, condensates begin forming in the atmospheres of ultracool dwarfs. In particular, titanium- and vanadium-bearing condensates form, resulting in a loss of TiO and VO from the gas (Lodders 2002); the weakening and eventual loss of the TiO and VO bands mark the transition to the L spectral class ($1400 \text{ K} \lesssim T_{\text{eff}} \lesssim 2400 \text{ K}$). With the loss of the TiO and VO bands, the resonant K I doublet becomes very prominent in the spectra of L dwarfs and eventually comes to define the continuum hundreds of angstroms from line center. In the near-infrared, the H₂O and CO bands strengthen with decreasing T_{eff} . Additional condensates, most notably Ca-, Al-, Fe-, Mg-, and Si-bearing species, also form and affect the emergent spectra of L dwarfs by altering the temperature/pressure profile of the atmosphere and contributing their own opacities. The near-infrared colors of the L dwarfs become progressively redder due to the formation of these condensates. At the lower end of this T_{eff} range, CH₄ becomes the dominant carbon-bearing species in the upper, coolest layers of the atmosphere, since CO/CH₄ < 1 for $T \lesssim 1100 \text{ K}$ at $P = 1$ bar (Lodders & Fegley 2002). Indeed, the ν_3 fundamental band of CH₄ at $3.3 \mu\text{m}$, which is ~ 100 times stronger than the combination and overtone bands in the near-infrared and ~ 10 times stronger than the ν_4 fundamental band in the mid-infrared, can be seen in the spectra of mid- to late-type L dwarfs.

As T_{eff} continues to decrease, CH₄ becomes ever more dominant over CO; the appearance of the CH₄ overtone and combination bands in the near-infrared signals the transition to the T spectral class ($600 \text{ K} \lesssim T_{\text{eff}} \lesssim 1400 \text{ K}$). The condensates that help

shape the spectral morphology of the L dwarfs form well below the observable photosphere in T dwarfs, resulting in a relatively condensate-free atmosphere. The strong H₂O and CH₄ bands carve the near-infrared spectra of T dwarfs up into narrow bands centered at 1.25, 1.6, and 2.2 μm . Finally, NH₃ becomes the dominant nitrogen-bearing gas, since N₂/NH₃ < 1 for $T \lesssim 700 \text{ K}$ at $P = 1$ bar (Lodders & Fegley 2002) and, consequently, the ν_2 fundamental band of NH₃ at $\sim 10.5 \mu\text{m}$ is present in the spectra of T dwarfs.

4.2. Bolometric Luminosities

The effective temperatures of ultracool dwarfs are typically determined by combining observed bolometric luminosities with theoretical radii (Leggett et al. 2001; Dahn et al. 2002; Golimowski et al. 2004). The bolometric luminosities are measured using absolutely flux-calibrated optical and near-infrared spectra, L' -band (and sometimes M' -band) photometry to account for the flux between ~ 2.5 and $\sim 4 \mu\text{m}$, and a Rayleigh-Jeans tail at $\lambda \gtrsim 4 \mu\text{m}$. Although Cushing et al. (2005) have shown that L' -band photometry can be used as a substitute for spectroscopy from 2.9 to 4.1 μm for spectral types ranging from M1 to T4.5, the assumption of a Rayleigh-Jeans tail at $\lambda \gtrsim 4 \mu\text{m}$ has never been tested observationally. The IRS spectra are ideal for this purpose.

Twelve of the dwarfs in our sample have both published absolutely flux-calibrated 0.6–4.1 μm spectra (Cushing et al. 2005) and IRS spectra. In order to construct spectra suitable for integration over all wavelengths, we modified each spectrum by linearly interpolating from zero flux at zero wavelength to its bluest wavelength and removing the gaps in wavelength coverage from 1.85 to 2.6 μm and 4.1 to 5.5 μm by linear interpolation between the flux densities at the gap edges. Finally, we extend a Rayleigh-Jeans tail from the reddest wavelength of each spectrum to infinity. In order to perform as accurate a comparison as possible with the results of Golimowski et al. (2004), we use the same parallaxes and assume $M_{\text{bol},\odot} = +4.75$. The results are listed in Table 2 along with the values derived by Golimowski et al. (2004). We find that the bolometric magnitudes of the twelve dwarfs agree within the errors, except for 2MASS J1439+1929

(L1), which is discrepant by just over 1σ . The values of L_{bol} , and thus the values of T_{eff} , of the ultracoal dwarfs with spectral types ranging from M1 V to T4.5 presented by Golimowski et al. (2004) are therefore robust against any systematic errors introduced using photometry and a Rayleigh-Jeans to account for the flux between 2.5 and 15 μm .

5. SUMMARY

We have presented a spectroscopic sequence of M, L, and T dwarfs from 5.5 to 38 μm at $R \approx 90$ obtained with the IRS on board the *Spitzer Space Telescope*. The spectra exhibit prominent absorption bands of H_2O , CH_4 , and NH_3 , and are relatively featureless at $\lambda \gtrsim 15 \mu\text{m}$. H_2O absorption features are present throughout the MLT sequence, while the CH_4 and NH_3 bands first appear at roughly the L/T transition. We tentatively ascribe a plateau in the spectra of a number of mid-type L dwarfs from 9 to 11 μm to the effects of a population of small silicate grains, likely lying above the main cloud deck, that are not predicted in current cloud models. The spectrum of the mildly metal-poor, high surface gravity, T dwarf 2MASS J0937+2931 (T6p) is suppressed from 5.5 to 7.5 μm relative to typical T6 dwarfs, indicating that mid-infrared spectroscopy may be a useful probe of surface gravity and/or metallicity variations. Finally, we computed bolometric magnitudes for 12 of the dwarfs in our sample with previously published 0.6–4.1 μm spectra and find good agreement with the values of Golimowski et al., who use L' - and M' -band photometry to account for the flux emitted at $\lambda > 2.5 \mu\text{m}$.

We thank Brian Patten for providing the IRAC Band 4 observations in advance of publication, Peter Hauschildt for providing the AMES-COND synthetic spectra, John Rayner for providing the near-infrared spectrum of GJ 1111 in advance of publication, and Richard Freedman, Katherina Lodders, Diane Wooden, Kelle Cruz, J. D. Smith, and William Vacca for useful discussions. This publication makes use of data from the Two Micron All Sky Survey, which is a joint project of the University of Massachusetts and the Infrared Processing and Analysis Center, and funded by the National Aeronautics and Space Administration and the National Science Foundation; the SIMBAD database, operated at CDS, Strasbourg, France; NASA's Astrophysics Data System Bibliographic Services; the M, L, and T dwarf compendium housed at DwarfArchives.org and maintained by Chris Gelino, Davy Kirkpatrick, and Adam Burgasser; and the NASA/IPAC Infrared Science Archive, which is operated by the Jet Propulsion Laboratory, California Institute of Technology, under contract with the National Aeronautics and Space Administration. This work is based (in part) on observations made with the *Spitzer Space Telescope*, which is operated by the Jet Propulsion Laboratory, California Institute of Technology, under a contract with NASA and is supported (in part) by the US Department of Energy under contract W-7405-ENG-36, and NASA through the *Spitzer Space Telescope* Fellowship Program, through a contract issued by the Jet Propulsion Laboratory, California Institute of Technology, under a contract with NASA. T. L. R. acknowledges the support of NASA's Science Mission Directorate.

REFERENCES

- Ackerman, A. S., & Marley, M. S. 2001, *ApJ*, 556, 872
 Allard, F., Hauschildt, P. H., Alexander, D. R., Tamanai, A., & Schweitzer, A. 2001, *ApJ*, 556, 357
 Basri, G. 2000, *ARA&A*, 38, 485
 Basri, G., Marcy, G. W., & Graham, J. R. 1996, *ApJ*, 458, 600
 Borysow, A. 2002, *A&A*, 390, 779
 Borysow, A., & Frommhold, L. 1986, *ApJ*, 303, 495
 Burgasser, A. J. 2001, Ph.D. thesis, Caltech
 Burgasser, A. J., Burrows, A., & Kirkpatrick, J. D. 2006a, *ApJ*, 639, 1095
 Burgasser, A. J., Geballe, T. R., Leggett, S. K., Kirkpatrick, J. D., & Golimowski, D. A. 2006b, *ApJ*, 637, 1067
 Burgasser, A. J., Kirkpatrick, J. D., Liebert, J., & Burrows, A. 2003, *ApJ*, 594, 510
 Burgasser, A. J., Kirkpatrick, J. D., & Lowrance, P. J. 2005a, *AJ*, 129, 2849
 Burgasser, A. J., Reid, I. N., Leggett, S. K., Kirkpatrick, J. D., Liebert, J., & Burrows, A. 2005b, *ApJ*, 634, L177
 Burgasser, A. J., et al. 2002, *ApJ*, 564, 421
 Burrows, A., Hubbard, W. B., Lunine, J. I., & Liebert, J. 2001, *Rev. Mod. Phys.*, 73, 719
 Burrows, A., & Sharp, C. M. 1999, *ApJ*, 512, 843
 Burrows, A., Sudarsky, D., & Hubeny, I. 2006, *ApJ*, 640, 1063
 Chabrier, G., & Baraffe, I. 2000, *ARA&A*, 38, 337
 Cohen, M., Megeath, S. T., Hammersley, P. L., Martín-Luis, F., & Stauffer, J. 2003, *AJ*, 125, 2645
 Creech-Eakman, M. J., Orton, G. S., Serabyn, E., & Hayward, T. L. 2004, *ApJ*, 602, L129
 Cruz, K. L., Reid, I. N., Liebert, J., Kirkpatrick, J. D., & Lowrance, P. J. 2003, *AJ*, 126, 2421
 Cushing, M. C., Rayner, J. T., & Vacca, W. D. 2005, *ApJ*, 623, 1115
 Cushing, M. C., Vacca, W. D., & Rayner, J. T. 2004, *PASP*, 116, 362
 Dahn, C. C., et al. 2002, *AJ*, 124, 1170
 Epchtein, N., et al. 1997, *Messenger*, 87, 27
 Fan, X., et al. 2000, *AJ*, 119, 928
 Fazio, G. G., et al. 2004, *ApJS*, 154, 10
 Fegley, B. J., & Lodders, K. 1996, *ApJ*, 472, L37
 Geballe, T. R., et al. 2002, *ApJ*, 564, 466
 Gizis, J. E., Monet, D. G., Reid, I. N., Kirkpatrick, J. D., Liebert, J., & Williams, R. J. 2000, *AJ*, 120, 1085
 Golimowski, D. A., et al. 2004, *AJ*, 127, 3516
 Hanner, M. S., Lynch, D. K., & Russell, R. W. 1994, *ApJ*, 425, 274
 Hawley, S. L., Gizis, J. E., & Reid, I. N. 1996, *AJ*, 112, 2799
 Helling, C., Thi, W.-F., Woitke, P., & Fridlund, M. 2006, *A&A*, 451, L9
 Henry, T. J., Kirkpatrick, J. D., & Simons, D. A. 1994, *AJ*, 108, 1437
 Herzberg, G. 1945, *Infrared and Raman Spectra of Polyatomic Molecules* (New York: Van Nostrand)
 Higdon, S. J. U., et al. 2004, *PASP*, 116, 975
 Houck, J. R., et al. 2004, *ApJS*, 154, 18
 Kirkpatrick, J. D. 2005, *ARA&A*, 43, 195
 Kirkpatrick, J. D., Dahn, C. C., Monet, D. G., Reid, I. N., Gizis, J. E., Liebert, J., & Burgasser, A. J. 2001, *AJ*, 121, 3235
 Kirkpatrick, J. D., Henry, T. J., & McCarthy, D. W. 1991, *ApJS*, 77, 417
 Kirkpatrick, J. D., Henry, T. J., & Simons, D. A. 1995, *AJ*, 109, 797
 Kirkpatrick, J. D., et al. 1999, *ApJ*, 519, 802
 ———. 2000, *AJ*, 120, 447
 Knapp, G. R., et al. 2004, *AJ*, 127, 3553
 Leggett, S. K., Allard, F., Dahn, C., Hauschildt, P. H., Kerr, T. H., & Rayner, J. 2000, *ApJ*, 535, 965
 Leggett, S. K., Allard, F., Geballe, T. R., Hauschildt, P. H., & Schweitzer, A. 2001, *ApJ*, 548, 908
 Leggett, S. K., et al. 2002, *ApJ*, 564, 452
 Lodders, K. 1999, *ApJ*, 519, 793
 ———. 2002, *ApJ*, 577, 974
 Lodders, K., & Fegley, B. 2002, *Icarus*, 155, 393
 Marley, M. 2000, in *ASP Conf. Ser. 212, From Giant Planets to Cool Stars*, ed. C. A. Griffith & M. S. Marley (San Francisco: ASP), 152
 Marley, M. S., Seager, S., Saumon, D., Lodders, K., Ackerman, A. S., Freedman, R. S., & Fan, X. 2002, *ApJ*, 568, 335
 Matthews, K., Nakajima, T., Kulkarni, S. R., & Oppenheimer, B. R. 1996, *AJ*, 112, 1678
 McLean, I. S., McGovern, M. R., Burgasser, A. J., Kirkpatrick, J. D., Prato, L., & Kim, S. S. 2003, *ApJ*, 596, 561
 Nakajima, T., Oppenheimer, B. R., Kulkarni, S. R., Golimowski, D. A., Matthews, K., & Durrance, S. T. 1995, *Nature*, 378, 463
 Noll, K. S., Geballe, T. R., Leggett, S. K., & Marley, M. S. 2000, *ApJ*, 541, L75
 Noll, K. S., Geballe, T. R., & Marley, M. S. 1997, *ApJ*, 489, L87
 Oppenheimer, B. R., Kulkarni, S. R., Matthews, K., & van Kerkwijk, M. H. 1998, *ApJ*, 502, 932
 Patten, B., et al. 2006, *ApJ*, in press (astro-ph/0606432)
 Perryman, M. A. C., et al. 1997, *A&A*, 323, L49
 Reach, W. T., et al. 2005, *PASP*, 117, 978
 Rebolo, R., Martín, E. L., Basri, G., Marcy, G. W., & Zapatero-Osorio, M. R. 1996, *ApJ*, 469, L53
 Rebolo, R., Zapatero Osorio, M. R., Madruga, S., Bejar, V. J. S., Arribas, S., & Licandro, J. 1998, *Science*, 282, 1309

- Reid, I. N., Kirkpatrick, J. D., Gizis, J. E., Dahn, C. C., Monet, D. G., Williams, R. J., Liebert, J., & Burgasser, A. J. 2000, *AJ*, 119, 369
- Roellig, T. L., et al. 2004, *ApJS*, 154, 418
- Saumon, D., Marley, M. S., & Lodders, K. 2003a, preprint (astro-ph/0310805)
- Saumon, D., Marley, M. S., Lodders, K., & Freedman, R. S. 2003b, in *IAU Symp. 211, Brown Dwarfs*, ed. E. Martín (San Francisco: ASP), 345
- Scholz, R.-D., McCaughrean, M. J., Lodieu, N., & Kuhlbrodt, B. 2003, *A&A*, 398, L29
- Skrutskie, M. F., et al. 2006, *AJ*, 131, 1163
- Stephens, D. C., Marley, M. S., Noll, K. S., & Chanover, N. 2001, *ApJ*, 556, L97
- Sterzik, M. F., et al. 2005, *A&A*, 436, L39
- Tinney, C. G., Burgasser, A. J., & Kirkpatrick, J. D. 2003, *AJ*, 126, 975
- Tinney, C. G., Reid, I. N., Gizis, J., & Mould, J. R. 1995, *AJ*, 110, 3014
- Toppani, A., Libourel, G., Robert, F., Ghanbaja, J., & Zimmermann, L. 2004, in *35th Lunar and Planetary Science Conf. Abstracts* (Houston: LPI), 1726
- van Altena, W. F., Lee, J. T., & Hoffleit, E. D. 1995, *The General Catalogue of Trigonometric Parallaxes* (4th ed.; New Haven: Yale Univ. Obs.)
- Vrba, F. J., et al. 2004, *AJ*, 127, 2948
- Weck, P. F., Schweitzer, A., Kirby, K., Hauschildt, P. H., & Stancil, P. C. 2004, *ApJ*, 613, 567
- Werner, M. W., et al. 2004, *ApJS*, 154, 1
- Wilson, J. C., Kirkpatrick, J. D., Gizis, J. E., Skrutskie, M. F., Monet, D. G., & Houck, J. R. 2001, *AJ*, 122, 1989
- Wilson, J. C., Miller, N. A., Gizis, J. E., Skrutskie, M. F., Houck, J. R., Kirkpatrick, J. D., Burgasser, A. J., & Monet, D. G., 2003, in *IAU Symp. 211, Brown Dwarfs*, ed. E. L. Martin (San Francisco: ASP), 197
- Woitke, P., & Helling, C. 2004, *A&A*, 414, 335
- York, D. G., et al. 2000, *AJ*, 120, 1579